Key Engineering Materials
ISSN: 1662-9795, Vol. 926, pp 2293-2302
doi:10.4028/p-9ur6l9

Submitted: 2021-12-13
Accepted: 2022-02-21
Online: 2022-07-22

Numerical Investigation of Influence of Spot Geometry in Laser Peen Forming of Thin-Walled Ti-6Al-4V Specimens

Dominik Pöltl[1,a,*], Sören Keller[2,b], Sergey Chupakhin[3,c], Siva Teja Sala[2,d], Nikolai Kashaev[2,e] and Benjamin Klusemann[1,2,f]

[1]Leuphana University Lüneburg, Institute of Product and Process Innovation, Lüneburg, Germany

[2] Helmholtz-Zentrum Hereon, Institute of Materials Mechanics, Geesthacht, Germany

[3]ZAL Zentrum für Angewandte Luftfahrtforschung GmbH , Hamburg, Germany

[a]dominik.poeltl@leuphana.de, [b]Soeren.Keller@hereon.de, [c]sergey.chupakhin@zal.aero, [d]Siva.Sala@hereon.de, [e]nikolai.kashaev@hereon.de, [f]Benjamin.Klusemann@leuphana.de

Keywords: Finite element analysis, laser peen forming, eigenstrain, laser focus, bending

Abstract. The aviation industry demands thin-walled structures of high dimensional accuracy. Varying radii and individual use-cases, e.g. for repair purpose, require flexible forming techniques. Laser peen forming (LPF) represents such a forming process providing precise energy input by a pulsed laser over a wide energy range. Among adjustable parameters such as laser intensity and focus size, the spot shape, i.e. square and circular, is usually fixed for a specific laser system. As the spot shape is a crucial parameter, this work focuses on the effect of the spot shape on structural deformation after LPF application. Therefore, models for laser peen forming of thin-walled Ti-6Al-4V strips for LPF systems with circular and square focus shapes are set up. Geometric conditions on both focus shapes ensure equal energy input during the laser processing. The numerical simulation relies on the so called eigenstrain method, leading to a cost-efficient calculation of resulting deformation after the dynamic LPF process. Square-based peening pattern exhibit higher deflection. For increasing spot size, the deflection difference between square and circle-based patterns increase slightly.

Introduction

Laser processing is a promising path to facilitate small forming operations such as adjusting small geometric inaccuracies after previous processing steps. While market-ready systems for laser peen forming (LPF) exist, this advanced forming method continues to be an active research field. Based on principles of laser processing [1], it offers various, yet highly controllable parameters to tailor desired shaping of a specimen. A peening pattern is generated as a sequence of single laser shots. For each single laser shot, the following dynamic unfolds: A high-powered pulsed laser with intensity in the GW/cm² regime and pulse duration in the nanosecond regime strikes a target's surface, generating a rapidly expanding plasma. This plasma is confined by a transparent layer, e.g. water, see Fig. 1 (a). The mechanical shock wave, stemming from the plasma and propagating through the specimen, causes dynamic yielding and introduces plastic strains, as illustrated in Fig. 1 (b), that lead to global deformation of the specimen. Hu et al. [2] investigated the dependency of bending on the laser power intensity and specimen thickness. Further work of Hu et al. [3] identified elastic prestress as a mean to further increase bending by LPF. The feasibility of LPF for composites such as fiber metal laminates has been demonstrated [4].

Commercial systems with circular as well as rectangular beam shapes are available, but due to high system prices, industrial applications as well as research groups typically stick to one of the two beam shapes. Therefore, this paper uses numerical simulations of the LPF process to assess the influence of the laser spot shape in combination with different pulse parameters and spot sizes. Thus, numerical simulation of laser processing can play out its advantages, delivering through-thickness stress data for advanced control of the forming operation and allowing for cheap examination of various parameters. Luo et al. [5] just recently treated the inverse problem of LPF, with a desired deflection as input and a LPF process strategy as an output.

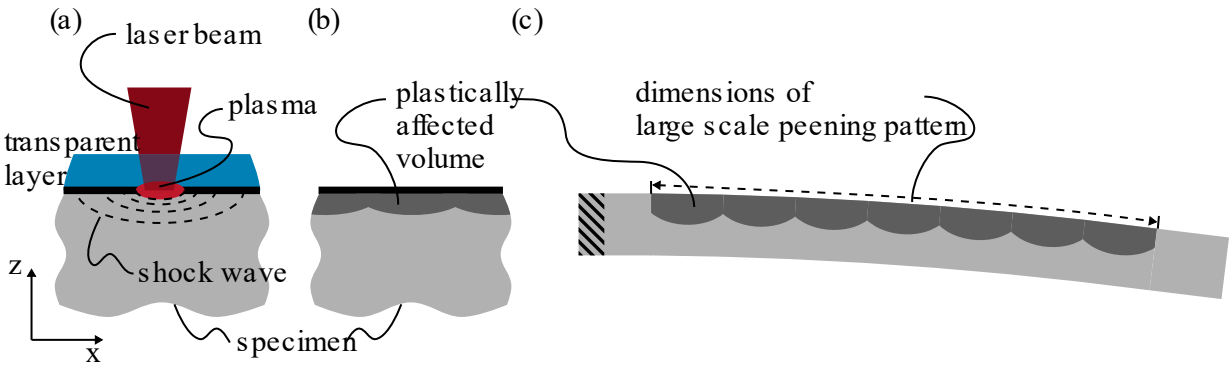

Figure 1: (a) The plasma, excited by the incoming laser beam and confined by the transparent layer, induces mechanical shock waves in the geometry. (b) After the laser processing, plastically affected volumes remain. (c) These plastically affected volumes lead to global deformation of a structure, as illustrated by stripe in the xz-plane.

Hfaiedh et al. [6] demonstrated how simulations resolve stress gradients, i.e. the driving forces behind bending moments, better than measurements. Hu et al. [7] numerically simulated LPF on 63 geometries with parameters in between to experimentally investigated ones, thus demonstrating the possible high density probing of parameter spaces.

Direct numerical simulation of laser processing requires great computational effort. The eigenstrain method proposes a drastic gain in computational efficiency [8]. Eigenstrain-based modeling was used by Hu et al. [3] to predict LPF of the aluminium alloy AA2024 under elastic prestress, while Keller et al. [9] and Sun et al. [10] applied the method to predict fatigue crack propagation in different C(T) specimens after laser shock peening.

The influence of spot shape on the equibiaxiality of the residual stress field is examined by Kallien et al. [11] for square spots and by Correa et al. [12] for circular spots. Yet, the materials, the overlaps and the spot sizes were different. This finally motivates the goal of this work to investigate the influence of spot shape and size for a constant set of other parameters. The material under investigation is Ti-6Al-4V representing one of the most used alloys with application in aerospace industry due to its high strength to weight ratio, the high corrosion resistance and high temperature stability [13].

Simulation Setup

Multi-step simulation strategy. The global deformation after larger scale LPF is reached via a three step finite element simulation strategy: (1) laser peening process simulation on a relative small volume, referred to as source geometry; (2) strain transfer by assuming periodicity of strains to a larger volume, referred to as target geometry; (3) calculation of stresses, strains and deflection of the target geometry, see Fig. 1 (c).

Plasma pressure. The laser peening process simulation calculates plastic strains caused by the plasma pressure acting on the material's surface. The plasma pressure is typically a function of time t and space x as $p(t, x, x_0)$, yet $\nabla_x p = 0$ is assumed in this work, i.e. $p(t)$. Various shapes of the temporal pressure function $p(t)$ are proposed in the literature: Early work from Brockmann et al. [14] proposed an analytical, triangular shape. Spradlin et al. [15] extended this shape with a plateau. Sticchi et. al [16] and Berthe et al. [17] modeled the pulse shape with discrete values according to experimental data. In this work, a temporal distribution $p(t)$, dubbed the *Shark* pulse, was used to account for two main characteristics: the short rise time (SRT), responsible for high induced strain rates, and the exponential decay, accounting for decaying pressure after the laser pulse ended. The Shark pulse is in good accordance with published experimental plasma pressure determinations, i.e. VISAR measurements [16], [17].

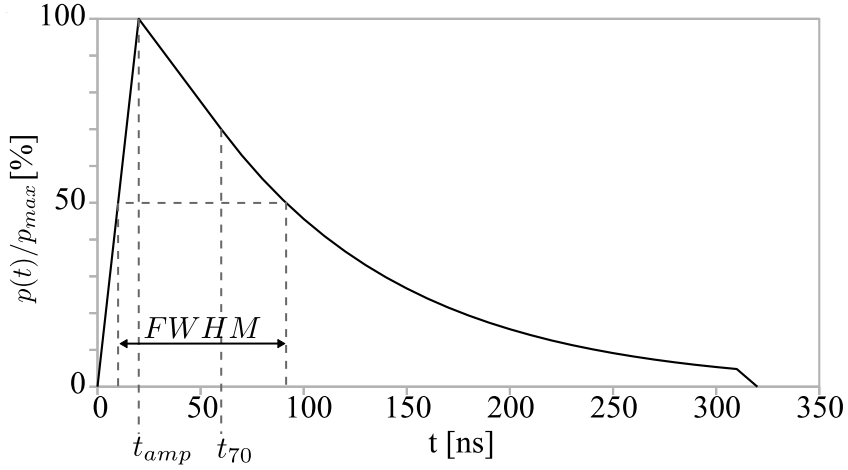

Figure 2: Normalized temporal distribution of the modeled plasma pressure pulse $p(t)/p_{max}$. The parameters are the maximal pressure p_{max}, the amplitude time t_{amp} and the time t_{70}s.t. $p(t_{70}) = 0.7p_{max}$. The decay is truncated for $p(t) \leq 0.05p_{max}$.

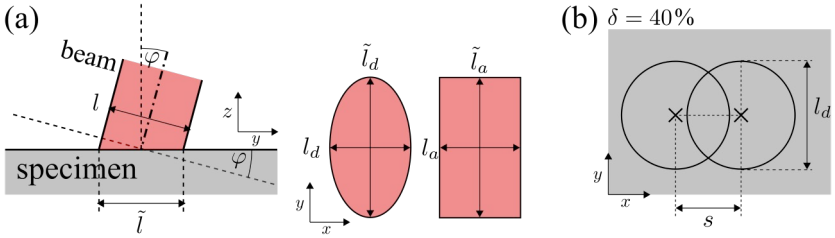

Figure 3: (a) The angle of attack φ, leading to a non-orthogonal projection of the beam shape onto the specimen's surface. (b) The step size s depends on the length l_d and the overlap δ.

Besides the two parameters maximal pressure p_{max} and amplitude time t_{amp} the introduced parameter t_{70}, denoting the time at which the pressure drops to 70% of its maximum value, allows control of the speed of decay and thus a tailorable full width half maximum FWHM(t_{amp}, t_{70}). Eq. 1 summarizes the characteristics of the Shark pulse, where the normalized, temporal pressure distribution is visualized in Figure 2.

$$\begin{aligned} p(t_{amp}) &= p_{max} \\ p(t_{70}) &= 0.7p_{max} \\ p(t) &\propto p_{max}\, exp(-t) \text{ for } t > t_{70} \end{aligned} \tag{1}$$

In this work, three pulses with thee maximal pressures of 1800 MPa, 2200 MPa and 3000 MPa as well as equal time parameters of 20 ns and of 60 ns were used. The time parameters result in a FWHM of 81 ns.

Peening pattern. A peening pattern is generated as a structured repetition of single peening spots. The single spot is described by a characteristic length l, e.g. the diameter l_d for a circular spot and the edge length l_a for a rectangular spot, and a non-zero angle of attack φ. a deviation from orthogonality to the peened surface to avoid reflections harmful to the peening system, see Fig. 3(a). While the non-orthogonal projection onto the specimen's surface for a non-zero angle of attack degenerates a circular laser beam into an elliptical spot and a square laser beam into a rectangular spot, the terms square and circle will be used throughout this paper for readability. Under an angle of attack φ, the characteristic length l along one axis will be stretched to $\tilde{l} = l/\,cos(\varphi)$. For all models, φ was set to 20°. The overlap δ describes how much of the connecting line between two center points of two consecutive single spots is covered by both their areas, see Fig. 3(b). The overlap in x and y direction can be different, yet were kept equal for all simulations in this paper.

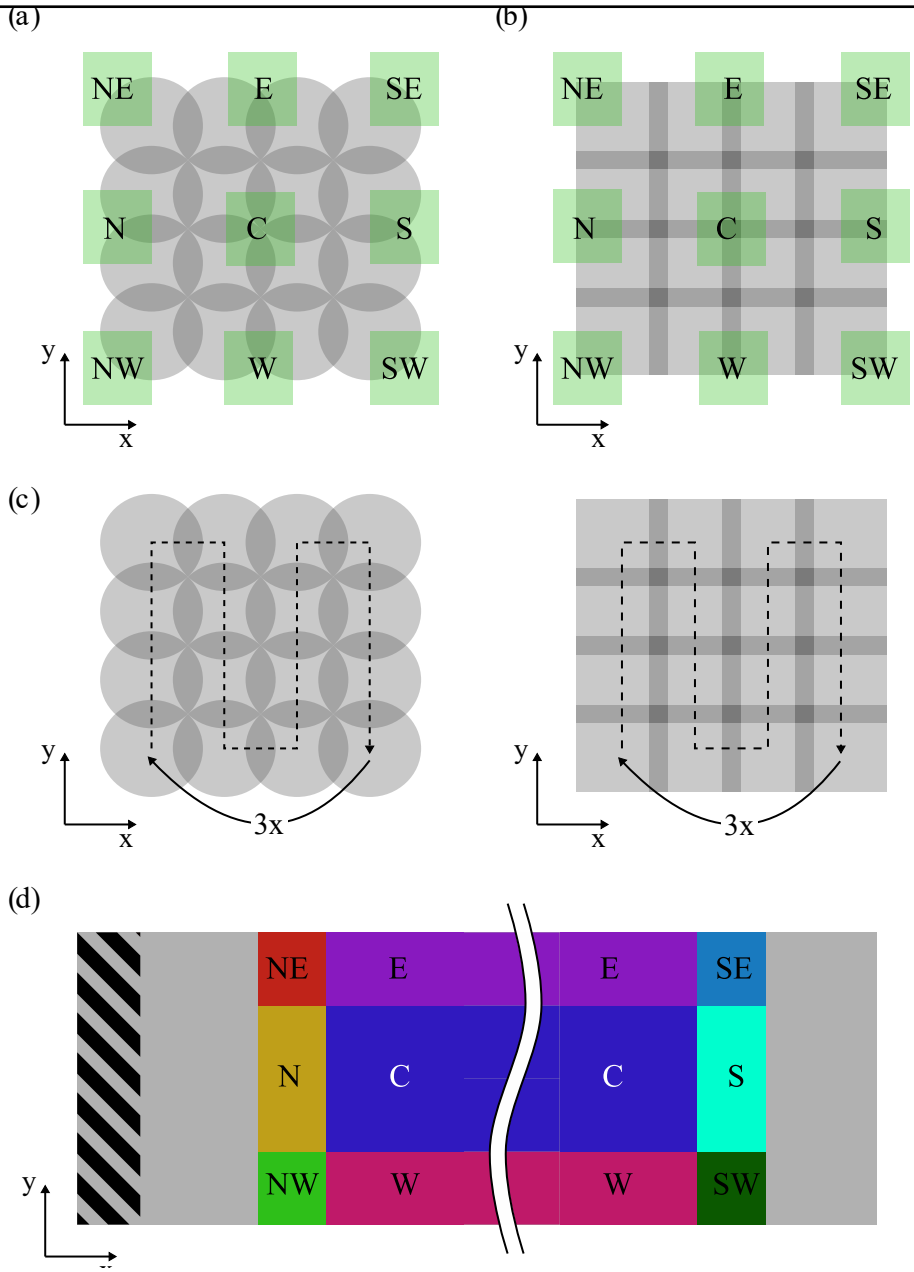

Figure 4: Peening pattern of 4×4 shots for (a) circular focus with critical overlap and (b) square focus with associated overlap. Positions and size of the wind rose patches are illustrated. (c) The chronological order of the peening process. (d) Tiling of a larger scale peening pattern with the 9 wind rose patches.

In order to compare square- and circle-based patterns, two conditions are derived:

(1) The single square spot has the same area as the single circular spot. (2) The overlap of the circle- and square-based pattern are chosen s.t. the stepping distance, which is the distance between two center points of two consecutive and adjacent single spots, see Fig. 3(b), is equal. Both conditions guarantee that the energy applied by the same pulse characteristic over patterns with equal dimensions is equal for square- and circle-based patterns. For a circular spot, the critical overlap, ensuring that every point in the irradiated area is peened at least once, is given as $\delta_{crit,d} = 1 - 1/\sqrt{(2)} \approx 29.29\%$. This leads to a corresponding overlap for the square spot of $\delta_{crit,a} = 1 - \sqrt{(2/\pi)} \approx 20.21\%$, ensuring that the same average energy density is applied for both spot shapes.

For every pattern and under the assumption of periodicity of the plastic strain field in the plane of peening, i.e. the xy-plane, a wind rose is devised, sectioning the source pattern into 9 identically shaped rectangular patches: one center patch (C), four edges (N, E, S, W) as well as four corners (NE, SE, SW, NW), see Fig. 4 (a,b). This expands on the idea of Hu and Grandhi [18]. The edge length s

of these patches is determined by the characteristic length of the single spot l and the overlap δ as $s = l(1 - \delta)$. The plastic strain profile along the specimen's thickness, i.e. the z axis, is non-periodical, so a discretization of 20 cells over the 1 mm thickness extends the patches to cells of 50 µm thickness.

Source Simulation

Material model. The constitutive modeling of Ti-6Al-4V must account for the extremely high strain rate during laser processing [19]. A linear elastic-viscoplastic material model is used, where the Johnson-Cook material model with neglected temperature term was employed [20]

$$\sigma_y = \left[A_{JC} + B_{JC}\varepsilon_p^{n_{JC}}\right] + \left[1 + C_{JC}\ \ln\left(\frac{\dot{\varepsilon}_p}{\dot{\varepsilon}_{p,0}}\right)\right].$$

where $\dot{\varepsilon}_p$ is the equivalent plastic strain, A_{JC}, B_{JC}, C_{JC}, n_{JC} and $\dot{\varepsilon}_{p,0}$ are material parameters, listed for Ti-6Al-4V in Table 1. [21]

Table 1: Elastic and Johnson-Cook material parameters for Ti-6Al-4V [21].

Density ρ, [g/cm³]	Young's modulus E, [MPa]	Poisson's ration ν, [-]	Yield strength A_{JC}, [MPa]
4.47	108500	0.33	728.7
Strain hardening coefficient B_{JC}, [MPa]	**Strain hardening exponent n_{JC}, [-]**	**Strain rate hardening coefficient C_{JC}, [-]**	**Reference strain rate $\dot{\varepsilon}_{p,0}$, [s^{-1}]**
498.4	0.28	$28 \cdot 10^{-3}$	$1 \cdot 10^{-5}$

For the simulation of all models, the finite element method (FEM) with continuous, three dimensional elements with reduced integration (C3D8R) was used.

The source geometry is a 50 mm×50 mm×1 mm plate with 4×4 shots placed in the center, where fixed boundary conditions are applied along the outside edges. A region of interest, which is 1.5 times as large as the pattern, was meshed with average element size of 0.1 mm×0.1 mm×0.05 mm, guaranteeing sufficient mesh independence, and 20 mesh layers along the thickness of the plate. Models with circle-based patterns of 1 mm, 2 mm and 3 mm diameter as well as models with the corresponding square-based patterns were set up.

Using ABAQUS/Explicit, three peening sequences in a chronological meandering order were simulated, see Fig. 4 (c). Transient behavior due to reflections was accounted for in the step time. A simulation using ABAQUS/Standard followed suit to ensure a static state. After both the explicit and implicit simulation, an element volume weighted averaging scheme was applied to determine average stress and plastic strain tensors for each of the 9×20 wind rose cells. Note that the shown standard deviation is an element volume weighted standard deviation over all elements identified to be in a cell used to calculate the volume weighted strain averages.

Target Simulation

The target geometry is a strip with dimensions 80 mm×20 mm×1 mm. Continuous, three dimensional elements with reduced integration (C3D8R) and an average size of 0.2 mm×0.2 mm×0.05 mm generated the mesh. For the target simulation, only the linear elastic material model is employed. To simulate the clamping, the surfaces within the first 10 mm in length are fixed, see schematic in Fig. 4(d). With a starting distance of 4 mm to the clamped region, a peening area of 60 mm×20 mm and

the critical overlap was peened. This pattern would consist of 2229 shots for 1mm, 549 shots for 2 mm and 243 shots for 3mm. Instead of simulating these shots in a direct approach, the 16 shots simulated on a source geometry represent between 1-7% of them, thus leading to a significant reduction of simulated laser shots; hence highlighting the efficiency of the eigenstrain method.

Results

Fig. 5 (a, b) shows the specimen's surface, where a region in the center of the circular spots exhibits tensile stress, while the square spots lack this. This phenomenon is known as the *residual stress hole.* Peyre and Fabbro [1] explain this with wave reflection at the spot edges and interference in the center, while Lu et. al. [22] propose theoretical methods to suppress this phenomenon.

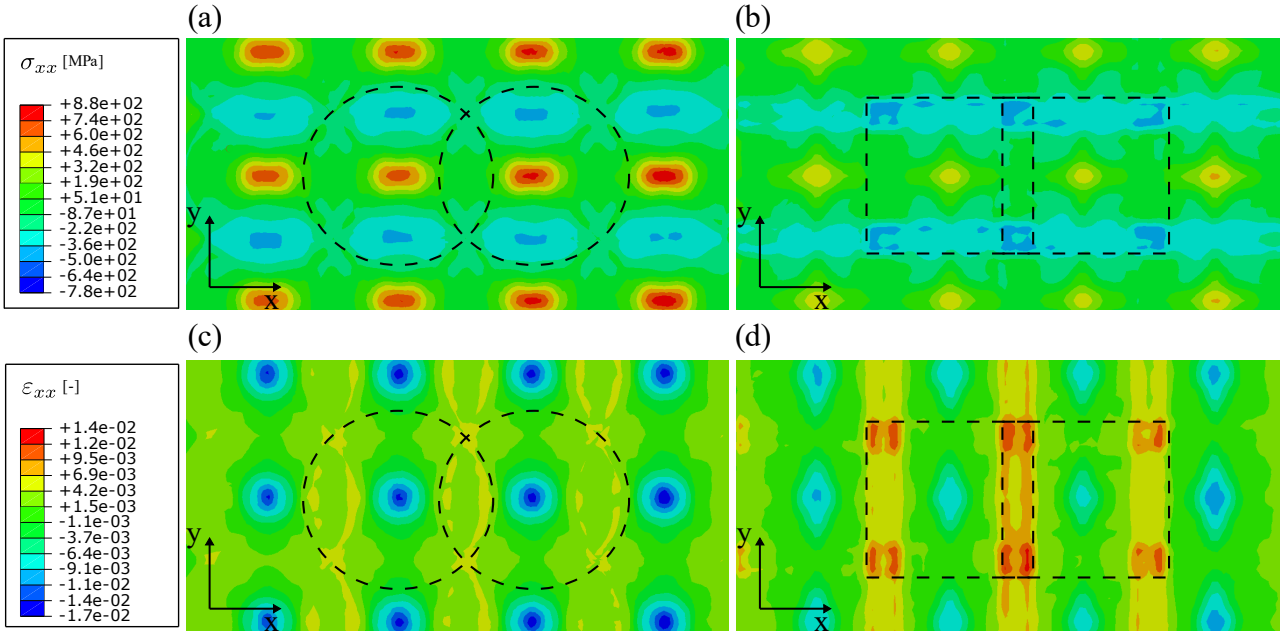

Figure 5: Field visualization for the surface of a source geometry after three layers of peening with a plasma pressure pulse with p_{max}=3000 MPa. (a) The in-plane stress component $\sigma_{xx}(z)$ for the circle-based pattern shows tensile stress in the spot center, (b) whereas the square-based center lacks this. (c) The in-plane plastic strain component $\varepsilon_{xx(z)}$ exhibits negative strains in the center, (d) whereas the square-based pattern exhibits dominant positive strains.

Although the energy input to the single spot and the whole irradiated area is equal, the stress profile along the material thickness exhibits differences between circle- and square-based pattern, see $\sigma_{xx}(z)$ for one parameter set in Fig. 6 (a). The deflection curves of the simulations are shown in Fig. 7. All circle-square pairs of equal spot area show differences in their deflection behavior. Three results are presented: For every spot size and every maximal pressure, square-based patterns exhibit higher deflection than circle-based patterns. This is supported by the plastic strain profile: the square-based pattern exhibits higher plastic strains than the circle-based pattern, see $\varepsilon_{xx}(z)$ for one parameter set in Fig. 6 (b). Only for the spot size $A = \pi/4(3\text{mm})^2$ and the highest maximal pressure of p_{max}=3000 MPa, the circle-based pattern exhibits stronger deflection than the square-based pattern. For constant maximal pressure and increasing spot size, the difference between the deflections of square and circle-based patterns increases slightly. For constant spot size and increasing maximal pressure, the difference between the deflection curves exhibits a weak increase. A convex deflection curve exhibits an angle $\theta_y < 0$ and is termed *downward* bending. In contrast, a concave deflection $\theta_y > 0$ is termed *upward* bending. The change from $\theta_y < 0$ to $\theta_y > 0$ is called bending mode change. The circle-based pattern exhibits a higher sensitivity towards a bending mode change: For p_{max}=2200 MPa, the square-based pattern exhibits downward/convex bending, while the circle-based pattern already experienced a bending mode change to upward/concave bending. For

p_{max}=3000 MPa, both patterns exhibit upward/concave bending. The tendency for a bending mode change with increasing maximal pressure p_{max} is supported by Hu et al. [2]. The intensity of the pressure pulse determines the local in-depth plastic strain distribution. Depending on the distribution, a positive or negative bending moment M_y is induced. As the specimen's thickness decreases, shock wave reflections and interference can be amplified with increasing maximal pressure.

The full-field data from the simulations can be used to examine the underlying driving forces for the differences in the bending behavior. This is the subject of future work.

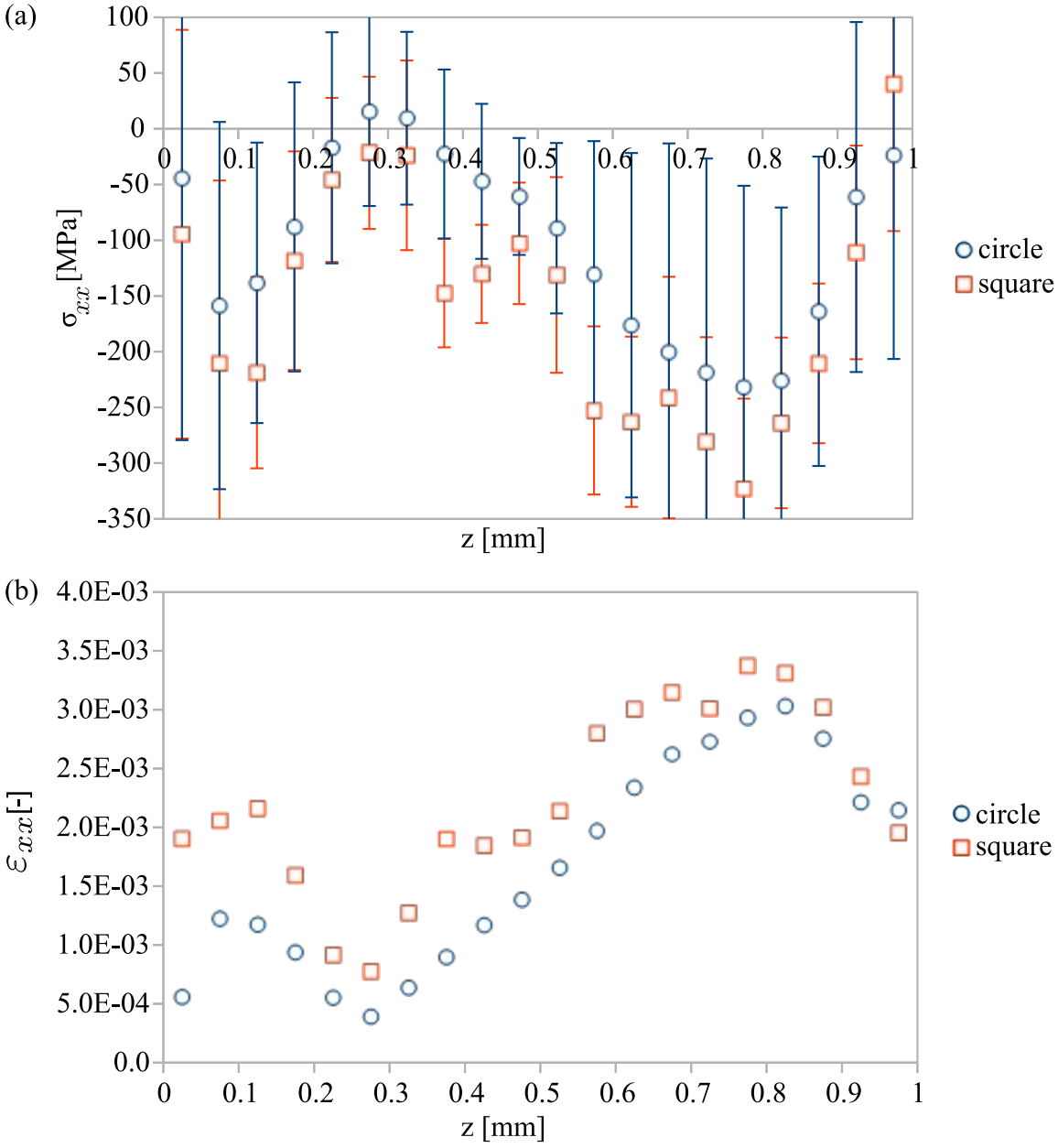

Figure 6: (a) stress profile $\sigma_{xx}(z)$ and (b) plastic strain profile $\varepsilon_{xx(z)}$ of center patch for circle-based and square based pattern with spot size $A = \pi/4(3\text{mm})^2$ after three layers of peening with a plasma pressure pulse with p_{max}=3000 MPa. The standard deviations for the plastic strain were omitted due to the high spatial gradients in the averaging area, see Fig. 5 (b) for a visualization.

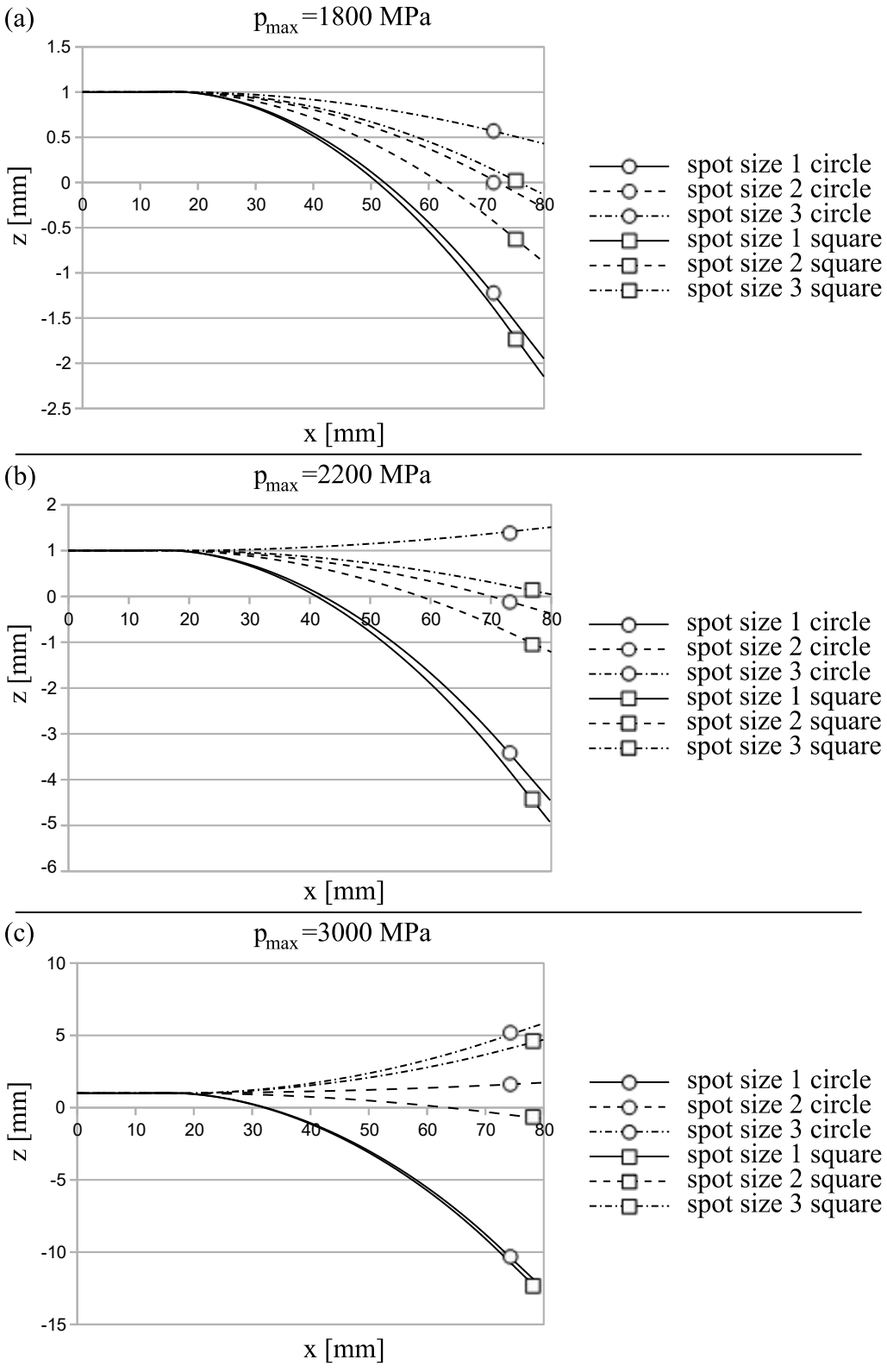

Figure 7: Bending curves of the 80 mm×20 mm×1 mm target geometry after simulated peening with a plasma pressure pulse with (a) p_{max}=1800 MPa, (b) p_{max}=2200 MPa and (c) p_{max}=30000 MPa for the circular and rectangular spot with increasing spot area : spot size 1 has $A = \pi/4(1\text{mm})^2$, spot size 2 has $A = \pi/4(2\text{mm})^2$, spot size 3 has $A = \pi/4(3\text{mm})^2$.

Conclusions

The objective of this work is the examination of the influence of spot geometry in laser peen forming (LPF) of 1 mm thick strips of Ti-6Al-4V. Peening patterns with square and circular spots and varying characteristic length are devised to allow for comparison. Models for LPF with the patterns are set up. The simulation strategy assumes an in-plane periodic plastic strain field, thus uses the eigenstrain method and follows three main steps: 1. explicit simulation of the laser process on a relatively small geometry, 2. transfer of plastic strains, averaged in representative cells, as thermal strains onto a larger scale target geometry, 3. simulation of bending of the target geometry due to thermal strains.

Based on the simulative results, the following conclusions are made:

- Eigenstrain approach requires simulation of <7% of the laser pulses of a direct process simulation
- Circle-based patterns exhibit significant tensile residual stresses in the spot centers on the surface.
- Square-based patterns lead to higher deflection than circle-based patterns.
- For increasing spot size, the deflection difference between square and circle-based patterns increases slightly.
- For increasing maximal pressure, the deflection difference between square- and circle-based patterns remains near constant.

The proposed simulation strategy can be adopted for more complex LPF applications. The simulation of LPF to adjust curved geometries to a given complex shape is an interesting future application of the eigenstrain method.

Funding

The work was carried out within the PEENCOR project funded by the German Federal Ministry of Economics and Technology (BMWi) under the LuFo VI-1 program (project numbers: 20Q1920A, 20Q1920C, 20Q1920D), which is gratefully acknowledged.

References

[1] P. Peyre and R. Fabbro, “Laser shock processing: a review of the physics and applications,” *Opt. Quantum Electron.*, vol. 27, no. 12, pp. 1213–1229, Dec. 1995, doi: 10.1007/BF00326477.

[2] Y. Hu, X. Xu, Z. Yao, and J. Hu, “Laser peen forming induced two way bending of thin sheet metals and its mechanisms,” *J. Appl. Phys.*, vol. 108, no. 7, p. 073117, Oct. 2010, doi: 10.1063/1.3486218.

[3] Y. Hu, Z. Li, X. Yu, and Z. Yao, “Effect of elastic prestress on the laser peen forming of aluminum alloy 2024-T351: Experiments and eigenstrain-based modeling,” *J. Mater. Process. Technol.*, vol. 221, pp. 214–224, Jul. 2015, doi: 10.1016/j.jmatprotec.2015.02.030.

[4] Y. Hu, X. Zheng, D. Wang, Z. Zhang, Y. Xie, and Z. Yao, “Application of laser peen forming to bend fibre metal laminates by high dynamic loading,” *J. Mater. Process. Technol.*, vol. 226, pp. 32–39, Dec. 2015, doi: 10.1016/j.jmatprotec.2015.07.003.

[5] M. Luo, Y. Hu, L. Hu, and Z. Yao, “Efficient process planning of laser peen forming for complex shaping with distributed eigen-moment,” *J. Mater. Process. Technol.*, vol. 279, p. 116588, May 2020, doi: 10.1016/j.jmatprotec.2020.116588.

[6] N. Hfaiedh, P. Peyre, I. Popa, V. Vignal, and W. Seiler, “Experimental and Numerical Analysis of the Distribution of Residual Stresses Induced by Laser Shock Peening in a 2050-T8 Aluminium Alloy,” *Mater. Sci. Forum*, vol. 681, pp. 296–302, Mar. 2011, doi: 10.4028/www.scientific.net/MSF.681.296.

[7] Y. Hu, Y. Xie, D. Wu, and Z. Yao, “Quantitative evaluation of specimen geometry effect on bending deformation of laser peen forming,” *Int. J. Mech. Sci.*, vol. 150, pp. 404–410, Jan. 2019, doi: 10.1016/j.ijmecsci.2018.10.040.

[8] H. K. Amarchinta, R. V. Grandhi, A. H. Clauer, K. Langer, and D. S. Stargel, “Simulation of residual stress induced by a laser peening process through inverse optimization of material models,” *J. Mater. Process. Technol.*, vol. 210, no. 14, pp. 1997–2006, Nov. 2010, doi: 10.1016/j.jmatprotec.2010.07.015.

[9] S. Keller, M. Horstmann, N. Kashaev, and B. Klusemann, “Experimentally validated multi-step simulation strategy to predict the fatigue crack propagation rate in residual stress fields after laser shock peening,” *Int. J. Fatigue*, vol. 124, pp. 265–276, Jul. 2019, doi: 10.1016/j.ijfatigue.2018.12.014.

[10] R. Sun, S. Keller, Y. Zhu, W. Guo, N. Kashaev, and B. Klusemann, “Experimental-numerical study of laser-shock-peening-induced retardation of fatigue crack propagation in Ti-17 titanium alloy,” *Int. J. Fatigue*, vol. 145, p. 106081, Apr. 2021, doi: 10.1016/j.ijfatigue.2020.106081.

[11] Z. Kallien, S. Keller, V. Ventzke, N. Kashaev, and B. Klusemann, “Effect of Laser Peening Process Parameters and Sequences on Residual Stress Profiles,” *Metals*, vol. 9, no. 6, p. 655, Jun. 2019, doi: 10.3390/met9060655.

[12] C. Correa *et al.*, “Random-type scanning patterns in laser shock peening without absorbing coating in 2024-T351 Al alloy: A solution to reduce residual stress anisotropy,” *Opt. Laser Technol.*, vol. 73, pp. 179–187, Oct. 2015, doi: 10.1016/j.optlastec.2015.04.027.

[13] R. R. Boyer, “An overview on the use of titanium in the aerospace industry,” *Int. Symp. Metall. Technol. Titan. Alloys*, vol. 213, no. 1, pp. 103–114, Aug. 1996, doi: 10.1016/0921-5093(96)10233-1.

[14] R. A. Brockman *et al.*, “Prediction and characterization of residual stresses from laser shock peening,” *Int. J. Fatigue*, vol. 36, no. 1, pp. 96–108, Mar. 2012, doi: 10.1016/j.ijfatigue.2011.08.011.

[15] T. J. Spradlin, R. V. Grandhi, and K. Langer, “Experimental validation of simulated fatigue life estimates in laser-peened aluminum,” *Int. J. Struct. Integr.*, vol. 2, no. 1, pp. 74–86, Jan. 2011, doi: 10.1108/17579861111108635.

[16] M. Sticchi *et al.*, “A parametric study of laser spot size and coverage on the laser shock peening induced residual stress in thin aluminium samples,” *J. Eng.*, vol. 2015, no. 13, pp. 97–105, May 2015, doi: 10.1049/joe.2015.0106.

[17] L. Berthe, R. Fabbro, P. Peyre, L. Tollier, and E. Bartnicki, “Shock waves from a water-confined laser-generated plasma,” *J. Appl. Phys.*, vol. 82, no. 6, pp. 2826–2832, Sep. 1997, doi: 10.1063/1.366113.

[18] Y. Hu and R. V. Grandhi, “Efficient numerical prediction of residual stress and deformation for large-scale laser shock processing using the eigenstrain methodology,” *Surf. Coat. Technol.*, vol. 206, no. 15, pp. 3374–3385, Mar. 2012, doi: 10.1016/j.surfcoat.2012.01.050.

[19] Z. Zhou *et al.*, “Thermal relaxation of residual stress in laser shock peened Ti–6Al–4V alloy,” *Surf. Coat. Technol.*, vol. 206, no. 22, pp. 4619–4627, Jun. 2012, doi: 10.1016/j.surfcoat.2012.05.022.

[20] G. R. Johnson and W. H. Cook, “A Constitutive Model and Data for Metals Subjected to Large Strains, High Strain Rates, and High Temperatures. Proceedings of the 7th International Symposium on Ballistic,” The Hague, Apr. 1983, pp. 541–547.

[21] W.-S. Lee and C.-F. Lin, “High-temperature deformation behaviour of Ti6Al4V alloy evaluated by high strain-rate compression tests,” *J. Mater. Process. Technol.*, vol. 75, no. 1, pp. 127–136, Mar. 1998, doi: 10.1016/S0924-0136(97)00302-6.

[22] G. Lu *et al.*, “Methods for the suppression of ‘residual stress holes’ in laser shock treatment,” *Mater. Today Commun.*, vol. 28, p. 102486, Sep. 2021, doi: 10.1016/j.mtcomm.2021.102486.